



Early-stage NiCrMo oxidation revealed by cryo-transmission electron microscopy



Alex Y.W. Lin^a, Alexander Müller^b, Xiao-xiang Yu^a, Andrew M. Minor^{b,c}, Laurence D. Marks^{a,*}

^a Department of Materials Science and Engineering, Northwestern University, Evanston, IL 60208, USA

^b National Center for Electron Microscopy, Molecular Foundry, Lawrence Berkeley National Laboratory, Berkeley, CA 94720, USA

^c Department of Materials Science and Engineering, University of California, Berkeley, CA 94720, USA

ARTICLE INFO

Keywords:

Cryo-transmission electron microscopy
Cryo-focused ion beam milling
Corrosion
Hydroxide growth
Sample preparation

ABSTRACT

Hydroxide formation at the surface of corroded alloys is critical for understanding early-stage oxidation of many corrosion-resistant alloys. Many hydroxides are unstable in an ambient environment and are electron-beam sensitive, limiting the use of conventionally-prepared specimens for transmission electron microscopy characterization of these alloy-water interfaces. In order to avoid sample dehydration, NiCrMo alloys corroded in a Cl⁻-containing electrolyte solution were cryo-immobilized by plunge freezing. A cryo-focused ion beam microscope was used to thin the sample to electron transparency, while preserving the alloy-water interface, and the sample was then cryo-transferred to a transmission electron microscope for imaging and diffraction. The presence of rocksalt Ni_{1-x}Cr_{2x/3}O and β-Ni_{1-x}Cr_{2x/3}(OH)₂ phases and their orientational relationship to the underlying alloy were observed with electron diffraction, confirming the preservation of the surface structure through the fully-cryogenic sample preparation and analysis.

1. Introduction

Nanoscale processes at solid-liquid interfaces play a critical role in many biological, chemical, and physical processes, ranging from fundamental phenomena such as crystal nucleation and growth in solution and hydrogels to more complex ones such as electrochemical changes of metal/alloy surfaces during aqueous corrosion or the formation of solid-electrolyte interfaces (SEI) in batteries. The understanding of real-time nanoscale processes at these interfaces remains largely limited owing to the difficult nature of observing these phenomena operando. While *in situ* investigations of aqueous corrosion have been conducted with Raman spectroscopy [1–3], X-ray spectroscopy [4–7], atomic force microscopy [8–10], scanning tunneling microscopy [11–14], and the surface force apparatus [15], these studies do not simultaneously acquire chemical and spatial information at sufficient resolutions to identify surface oxides and hydroxides or minor chemical changes at the metal-oxide interface. More recently, liquid cell transmission electron microscopy (TEM) has been used for *in situ* TEM characterizations of electrochemical reactions such as lithiation [16–19], SEI formation [20–22], and aqueous corrosion [23, 24]. However, the high current density of the electron beam is extremely reducing [25] and can impact electrochemical processes. In consequence, electron beam effects have to be limited, resulting in a reduction of spatial resolution due to a

reduced beam current. A recent appraisal [26] concluded that sub-nanometer spatial resolutions have not yet been achieved for *in situ* electrochemical experiments in the TEM.

Cryo-TEM avoids many of the problems described above and allows for the nanoscale characterization of the phases formed during early-stage aqueous corrosion by probing frozen, hydrated samples. Plunge freezing, a technique well-established for biological samples, is the process of rapidly freezing specimens in liquid ethane to prevent the transformation of water to the hexagonal ice phase and thereby preserve the near-native structure [27–30]. However, the specimens frozen with plunge freezing often will not be electron-transparent, as the formed ice layer is far too thick. Blotting can be used to reduce the thickness of the ice layer, but it is not reliable and often requires many attempts to produce a thin ice layer, especially when the form factor of a TEM sample changes. To overcome this, cryo-focused ion beam (FIB) can be used to thin and polish away excess ice to expose the interface between the corroded alloy and the electrolyte (see Methods and Materials), allowing the oxide and hydroxide phases at the interface to be examined with cryo-TEM [31, 32].

In this study, we will examine the early-stage aqueous corrosion of a NiCrMo alloy. It is well known that the addition of Mo to NiCr-based alloys inhibits the breakdown of passive films during aqueous corrosion, improving corrosion resistance [33–37]. During aqueous

* Corresponding author.

E-mail address: l-marks@northwestern.edu (L.D. Marks).

<https://doi.org/10.1016/j.ultramic.2019.01.012>

Received 27 September 2018; Received in revised form 14 January 2019; Accepted 20 January 2019

Available online 10 February 2019

0304-3991/ © 2019 Elsevier B.V. All rights reserved.

corrosion, different oxides and hydroxides form at the alloy surface. For instance, rocksalt NiO is commonly reported to form on corroded Ni metal and Ni-based alloys with a cube-on-cube epitaxial relationship [38–40]. With high-resolution electron microscopy (HREM), electron energy-loss spectroscopy (EELS) and atom-probe tomography analyses of corroded and oxidized NiCrMo alloys, the surface oxides were determined as a combination of rocksalt and corundum crystal structures with Ni, Cr, and traces of Mo in the rocksalt and Ni and Cr in the corundum due to nonequilibrium solute capture [41]. As previous studies have shown that corundum Cr_2O_3 has a larger thermodynamic driving force than NiO in Ni-based alloys [42], these experimental observations contradict the assumption that the most thermodynamically stable oxide forms first. Instead the composition of the oxide is determined by the growth rate at the metal-oxide interface, and local thermodynamic equilibrium is not present. What is not known in detail is to what extent stable hydroxides and oxyhydroxides [43–45] form near the surface in aqueous conditions, and any crystallographic relationships to the oxide or metal. Here, we present a workflow allowing for the preservation of the metal-electrolyte interface of NiCrMo alloy samples, and subsequent cryo-TEM characterization of the oxides and hydroxides in the near-native hydrated state, observing the early-stage aqueous corrosion in these corrosion-resistant alloys.

2. Methods and materials

2.1. Sample preparation

A Ni-22Cr-6Mo alloy was cut into discs with a diameter of 3 mm and a thickness of ~ 0.5 mm using a rotary disc cutter (South Bay Technology Model 360), and were mechanically thinned to thicknesses of ~ 100 μm with silicon carbide lapping paper. The discs were mechanically dimpled (VCR Model D500i Dimpler) until their centers were ~ 25 μm thick. Then, each disc was cut into two halves using a wire saw (South Bay Technology Model 850) to make the thin edge of the sample (which contains the alloy-hydroxide-water interface) accessible to the Ga^+ beam of the FIB. If the disc was not sectioned, the edge would be obstructed by the top half of the disc during cryo-FIB milling. The samples were washed with acetone and thinned to electron transparency using the Ar^+ ion beam of a Fischione Model 1050 TEM Mill operated at 5 kV with a 6° milling angle for 2 h, followed by a final polish at 1 kV with a 2° milling angle for 1 h. Our choice of ion milling, rather than electropolishing here was deliberate. As detailed in the next section, the samples were deliberately corroded for a long time to obtain a quasi steady-state, relatively thin oxide. For this it is advantageous to have an initial, somewhat damaged surface which is removed during the corrosion treatment, rather than a semi-passivated surface after electropolishing which may have viscosity control agents at the surface.

2.2. Aqueous corrosion and freezing

The NiCrMo half-discs were corroded in 200 mL of a stock solution containing 0.1 M NaCl and 0.0001 M HCl in H_2O (pH ~ 4.0), with 5 μL of H_2O_2 (30% w/w) injected above the sample surface to increase the oxidation rate. The condition was verified to produce an electrochemical potential near +0.2 V versus a saturated calomel reference electrode (SCE), a potential within the passive region. In all cases, the samples were corroded for 10^4 s at room temperature. Then, they were removed from the aqueous solution, rapidly frozen via plunge freezing in liquid ethane [46], and transferred to a cryogenic grid box immersed in liquid nitrogen.

2.3. Cryo-FIB milling

Due to the added ice layer formed during freezing, the pre-thinned samples were too thick for direct TEM imaging, and FIB milling was

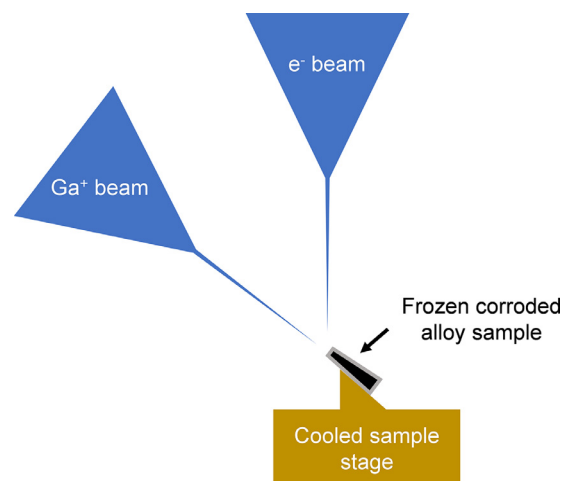


Fig. 1. Schematic showing the cryo-FIB milling process of a frozen, corroded NiCrMo alloy sample, which is mounted to the cooled stage in the FIB.

required to thin the samples and expose the oxide and hydroxide phases at the alloy-water interface. A Quorum PP3010T Cryo-FIB/SEM Preparation System, attached to a FEI Strata 235 dual-beam FIB, was used to image and mill the frozen alloy samples at low temperatures ($\leq -140^\circ\text{C}$). Firstly, the frozen samples were mounted into a Quorum 12406 sample shuttle such that the Ga^+ beam inside the FIB hits the sample at a glancing angle. Using a transfer rod keeping the sample in a nitrogen atmosphere, the shuttle was then transferred into a cryo-preparation chamber, which was operated at a pressure of 10^{-7} mbar and kept at -160°C to prevent a phase change to the hexagonal ice phase. Then, the shuttle was transferred into the FIB chamber through a connecting valve between the cryo-preparation chamber and the FIB and secured onto the stage kept at -160°C . We imaged the frozen alloy samples with a 5 kV electron beam prior to cryo-FIB milling. In contrast to the traditional TEM sample preparation using the FIB, where a series of cleaning cross-sections are completed on a single lamella, we selected regions along the thin ion-milled portion of the 3 mm half-disc and milled it from one side with a 30 kV Ga^+ ion beam. An illustration of the workflow inside the FIB is shown in Fig. 1. This milling method reduced the excess ice and the thickness of the alloy at the very edge of the sample and added notched markers for easier identification during cryo-TEM imaging. An ion beam current of 100 pA was initially used to line mill toward the sample with stage tilt angles of 5 – 10° , then the current was decreased stepwise down to 20 pA for the final cleaning step. The beam current values used have been shown to produce sufficiently thin lamellae of hydrogels and liquid-solid interfaces in oxide particles [47], demonstrating that the areas of interest at the alloy-water interface can be preserved with cryo-FIB milling.

2.4. Cryo-TEM characterization

The FIB milled sample was transferred to a cooled Gatan 915 double tilt cryo-transfer holder, which has a shutter to prevent the sample from being exposed to air during the transfer. Cryo-TEM characterization was performed on a FEI Titan TEM operated at 300 kV with a Gatan Orius 830 ($2k \times 2k$) CCD camera for diffraction pattern and image collection. Selected-area electron diffraction (SAED) patterns and corresponding dark field (DF) images from various regions of a polycrystalline diffraction ring were taken near the thin sample edge.

2.5. TEM characterization of conventionally-prepared specimens

For TEM characterization of conventionally-prepared specimens, the NiCrMo half-discs are dried in air after aqueous corrosion instead of plunge freezing the hydrated sample. Electron diffraction and high-

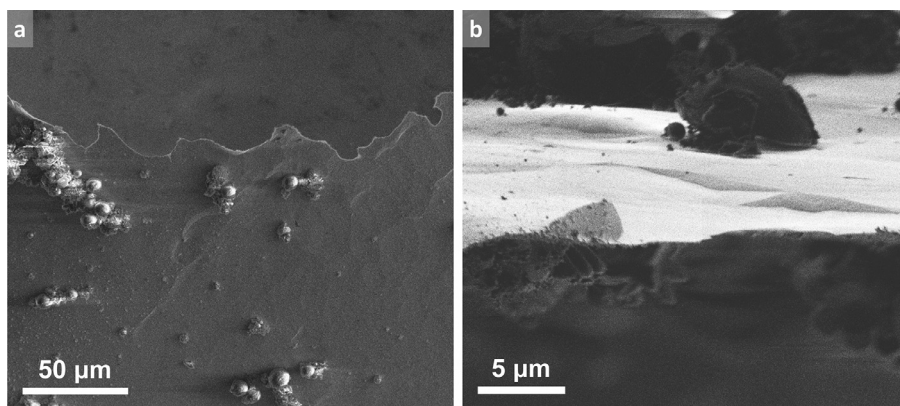


Fig. 2. (a) Cryo-SEM secondary electron image of the frozen corroded NiCrMo half-disc. The irregular top edge is the region that was pre-thinned to electron transparency with Ar^+ ion milling and the bright particles are ice crystals, which charge in the electron beam. (b) A top-down FIB secondary electron image of (a) shows that ice contamination (dark particles) is more significant in the lower part of the half-disc, away from the thin alloy edge.

resolution imaging of the dehydrated samples were performed on a JEOL 2100F TEM operated at 200 kV.

3. Results

When milling the sample, the ice layer resulted in the formation of a smooth surface, whereas the alloy showed significant curtaining. This allowed for easy identification of the two different materials during milling such that we could observe a 10–20 μm thick ice layer was preserved by plunge freezing. Such a thick layer would not be electron-beam transparent in the TEM, requiring it to be thinned. The cryo-FIB milling approach provided locally thin regions with smooth surfaces at the alloy-water interface. With SEM and FIB imaging of the NiCrMo half-disc, we observed minor ice contamination on the alloy surface (Fig. 2) that grew during the cryo-transfer processes. The FIB milling not only reduced the overall thickness of the vitreous ice layer, but also removed most of the small ice crystals in the regions of interest (Fig. 3). This allowed for characterization of the phases at the alloy-water interface during semi steady-state aqueous corrosion without extraneous scattering signals in images and diffraction patterns. As mentioned in the Methods and Materials section, several regions along the edge of the half-disc were thinned with the ion beam. In cryo-TEM images, the differences between FIB-milled and unmilled regions become more apparent (Fig. 4a). The FIB milled regions are electron-transparent and local diffraction contrast can be discerned, whereas adjacent regions are almost completely covered by ice which blocks the electron beam.

SAED patterns taken from the thinned region show that the alloy-oxide-hydroxide region was successfully preserved (Fig. 4b). In cryo-TEM images of milled regions, we only observe the presence of the native ice layer from the initial plunge freezing as opposed to hexagonal ice crystals. From SAED patterns of two different sites in the region shown in Fig. 4, we can conclude the presence of oxides, hydroxides,

and in some cases, vitreous ice. Specifically, polycrystalline diffraction rings indicate that the rocksalt $\text{Ni}_{1-x}\text{Cr}_{2x/3}\text{O}$ phase forms on the NiCrMo alloy surface, as expected from previous TEM characterizations of conventionally-prepared samples from the same alloy system [41] and similar oxidation experiments for Ni metal and other NiCr-based alloy systems [12, 13, 39, 48].

In addition to the rocksalt phase, polycrystalline $\beta\text{-Ni}_{1-x}\text{Cr}_{2x/3}(\text{OH})_2$ is identified in the SAED patterns. While we can be definitive that the crystal structure matches that of $\beta\text{-Ni}(\text{OH})_2$ we cannot exclude the strong possibility that Cr has been solute captured in the hydroxide, i.e. it is $\beta\text{-Ni}_{1-x}\text{Cr}_{2x/3}(\text{OH})_2$ [49, 50]. With DF imaging on the $\beta\text{-Ni}_{1-x}\text{Cr}_{2x/3}(\text{OH})_2$ polycrystalline diffraction rings, the location of $\beta\text{-Ni}_{1-x}\text{Cr}_{2x/3}(\text{OH})_2$ at the surface of the NiCrMo was confirmed (Fig. 5), suggesting that the hydrated alloy with the oxide and hydroxide phases is successfully preserved by the plunge freezing and cryo-FIB preparation process. The $\beta\text{-Ni}_{1-x}\text{Cr}_{2x/3}(\text{OH})_2$ phase was not observed in previous TEM characterizations of aqueous corrosion in conventionally-prepared Ni and NiCr specimens when the samples were dehydrated after corrosion. The DF images also indicate that the $\beta\text{-Ni}_{1-x}\text{Cr}_{2x/3}(\text{OH})_2$ crystallites, which are about 5–10 nm in diameter, form a layer at the edge of the alloy sample. Furthermore, some of the $\beta\text{-Ni}_{1-x}\text{Cr}_{2x/3}(\text{OH})_2$ crystallites are also distributed on the top surface of the alloy that lies parallel to the projection plane. As shown in Fig. 5c, many small $\beta\text{-Ni}_{1-x}\text{Cr}_{2x/3}(\text{OH})_2$ crystallites oriented in the (101) direction formed on the surface of the alloy bulk. This kind of crystallite distribution was not observed in the DF image of the $\beta\text{-Ni}_{1-x}\text{Cr}_{2x/3}(\text{OH})_2$ oriented in the (110) direction.

The $\beta\text{-Ni}(\text{OH})_2$ phase is a well-ordered phase which shows sharp diffraction peaks [51, 52]. For completeness, we should mention that there is one other hydroxide phase reported in the literature, $\alpha\text{-Ni}(\text{OH})_2$ [51, 52]. The $\alpha\text{-Ni}(\text{OH})_2$ phase is significantly more disordered, and shows broad diffraction features in the literature. As there is significant

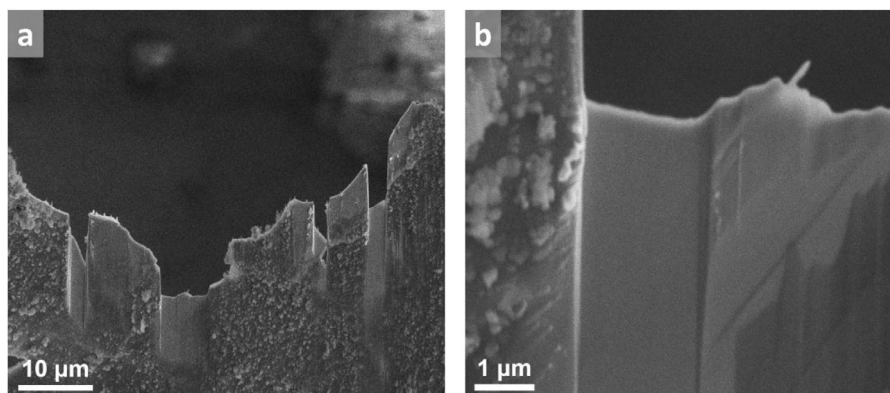
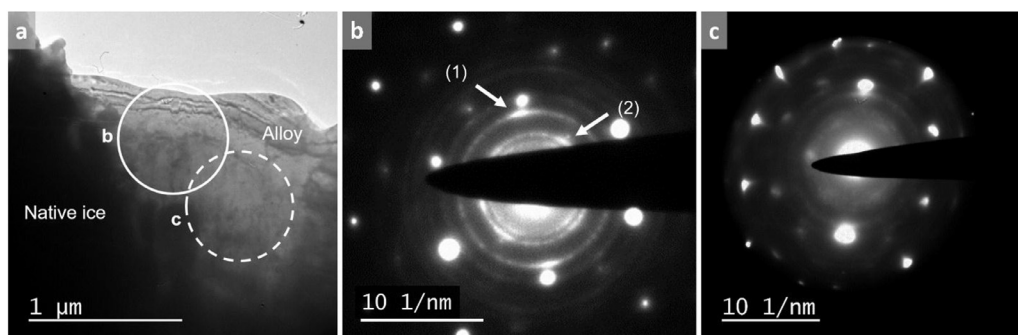


Fig. 3. Secondary electron image of (a) the cryo-FIB milled regions that also served as notched markers to identify regions of interest for cryo-TEM imaging. (b) Higher magnification image showing that the regions that were thinned have significantly less contamination in comparison with unthinned regions.



tion spots and (2) the (101) $\text{Ni}_{1-x}\text{Cr}_{2x/3}\text{O}$ ring and the (111) rocksalt diffraction spots are observed. (c) In the thicker part of the sample, the main diffraction spots that were observed in (b) are still visible but slightly shifted and distorted. The inner diffraction rings are more diffuse and correspond to vitreous ice and the major diffraction vectors of polycrystalline corundum.

overlap of the diffraction features with those of vitreous ice [28] and to some extent, $\beta\text{-Ni}(\text{OH})_2$ [45, 52], we cannot exclude the possible presence of some $\alpha\text{-Ni}_{1-x}\text{Cr}_{2x/3}(\text{OH})_2$ along with $\beta\text{-Ni}_{1-x}\text{Cr}_{2x/3}(\text{OH})_2$ in the samples. Since it is probable that hydroxides exist in the form of hydrogels prior to freezing, the $\text{Ni}(\text{OH})_2$ is probably trapped in a metastable state.

We can further conclude orientational relationships between $\beta\text{-Ni}_{1-x}\text{Cr}_{2x/3}(\text{OH})_2$, rocksalt, and the bulk alloy from the SAED patterns. The polycrystalline rings have an inhomogeneous intensity distribution, indicating preferential orientation of the $\beta\text{-Ni}_{1-x}\text{Cr}_{2x/3}(\text{OH})_2$ crystallites. The (110) diffraction ring of $\beta\text{-Ni}_{1-x}\text{Cr}_{2x/3}(\text{OH})_2$ in particular has intensity maxima near the (220) diffraction spots of Ni. In addition, we observe evidence of other orientational relationships from the weaker diffraction spots; for instance, the (101) $\beta\text{-Ni}_{1-x}\text{Cr}_{2x/3}(\text{OH})_2$ ring is more intense near the (111) rocksalt spots (Fig. 4b). This observation differs from previous diffraction studies of the cube-on-cube epitaxy between rocksalt and Ni [39] or NiCr alloys [41] in conventionally-prepared samples.

The characterization of conventionally-prepared samples was independently verified for this paper using the same aqueous corrosion treatment. Rocksalt $\text{Ni}_{1-x}\text{Cr}_{2x/3}\text{O}$ islands were observed with HREM on a corroded NiCrMo (Fig. 6a). Consistent with literature [39–41], electron diffraction of the islands showed that the rocksalt phase grew on the bulk Ni metal with a cube-on-cube epitaxy (Fig. 6b). In contrast to the cryo-TEM results of the frozen-hydrated sample as discussed earlier, the polycrystalline $\beta\text{-Ni}_{1-x}\text{Cr}_{2x/3}(\text{OH})_2$ phase was not observed in this non-cryogenic TEM sample preparation and characterization, indicating the need for a cryogenic approach to reveal the complex orientational relationships between the oxides and hydroxides with the bulk metal.

4. Discussion

The results presented indicate that it is possible to examine aqueous

corroded samples by a cryogenic approach, and obtain local structural information that is not accessible by other means. As observed in other studies, these samples are complex polycrystalline and non-conformal oxides/hydroxides, not the simple series of layers, all of equal thickness, commonly hypothesized in the literature [53–57]. While elements of the epitaxial arrangements are consistent with prior work in furnace oxidation [39] and aqueous corrosion [11–13], we have also identified a different type of epitaxy. In both cases, parallel cube-on-cube $\text{Ni}_{1-x}\text{Cr}_{2x/3}\text{O}$ on Ni epitaxy was observed in the passive oxide layer. Additionally, $\text{Ni}(\text{OH})_2$ was identified on Ni(111) single crystal surfaces in both alkaline and acidic solutions via *in situ* electrochemical STM, and the thickness and morphology of the hydroxide layer were determined to vary with the passivation potential [11]; in some cases there was probably an underlying oxide between the metal and the hydroxide which STM would not detect. While preferred orientations of the Ni(OH)₂ were not found for the electrochemical conditions of the study by Zuili et al. [11], we have identified two separate cases of preferred orientation for $\beta\text{-Ni}_{1-x}\text{Cr}_{2x/3}(\text{OH})_2$. In contrast to previous observations, where only amorphous granular $\text{Ni}(\text{OH})_2$ or a partial monolayer of the $\text{Ni}(\text{OH})_2$ (0001) basal plane were identified, we observed a polycrystalline $\beta\text{-Ni}_{1-x}\text{Cr}_{2x/3}(\text{OH})_2$ layer with $\beta\text{-Ni}_{1-x}\text{Cr}_{2x/3}(\text{OH})_2$ (101) crystallites preferentially oriented in the six-fold Ni (111) and rocksalt (111) direction, as well as $\beta\text{-Ni}_{1-x}\text{Cr}_{2x/3}(\text{OH})_2$ (110) crystallites that were preferentially oriented along the two-fold Ni (220). Electron diffraction of the hydroxide and the passive oxide layer has shown that the hydroxide conforms to the structure of the underlying passive layer. In agreement with previous studies of the lattice mismatch between NiO and $\text{Ni}(\text{OH})_2$ (7.5%) [11, 38, 44], the lattice mismatches for the two orientational relationships observed in this study were both between 5–7%. The crystallite sizes for $\beta\text{-Ni}_{1-x}\text{Cr}_{2x/3}(\text{OH})_2$, which range from 5–10 nm, are also in good agreement with previous studies of granular $\text{Ni}(\text{OH})_2$ structures, where grain sizes between 2 and 8 nm were measured [11].

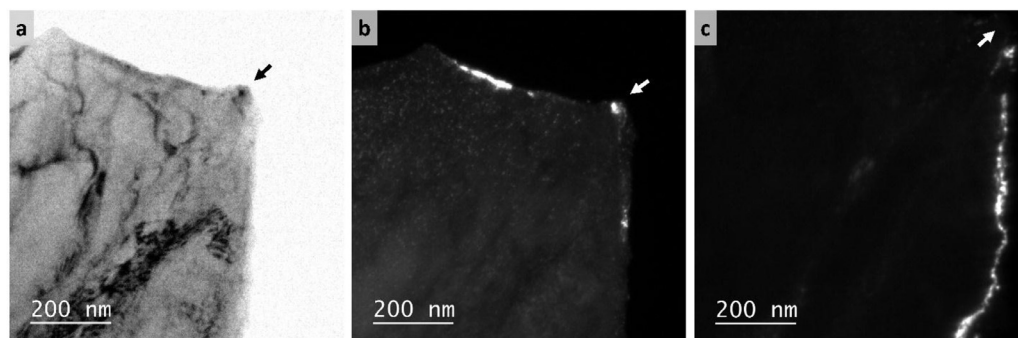


Fig. 5. (a) Bright-field and (b-c) corresponding dark-field TEM images of the edge of a frozen-hydrated NiCrMo sample. The DF images are formed using (b) the (101) $\beta\text{-Ni}_{1-x}\text{Cr}_{2x/3}(\text{OH})_2$ diffraction ring and (c) the (110) $\beta\text{-Ni}_{1-x}\text{Cr}_{2x/3}(\text{OH})_2$ diffraction ring. As indicated in both images, the $\beta\text{-Ni}_{1-x}\text{Cr}_{2x/3}(\text{OH})_2$ nanocrystals contributing to the diffraction lie on the edges of the Ni-alloy bulk, although some crystallites in the (101) direction are distributed on the surface of the bulk alloy, in addition to the sample edge. The arrow indicates the same location of the sample across each image.

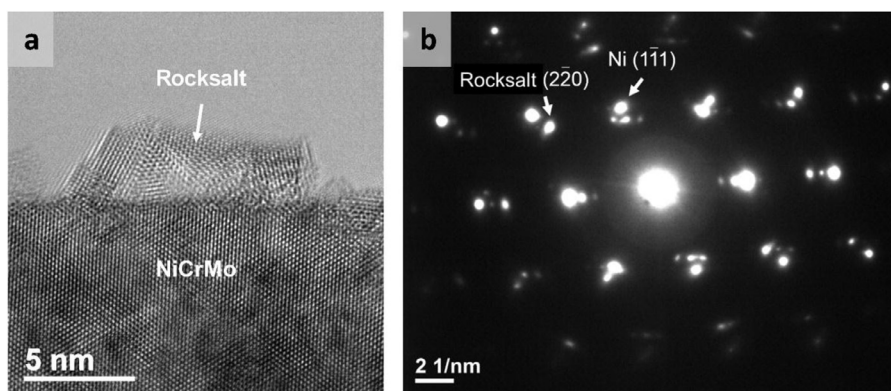


Fig. 6. (a) HREM image from a conventionally prepared (dehydrated) NiCrMo sample oxidized in 0.1 M NaCl and 0.0001 M HCl solution for 10^4 s shows the growth of rocksalt $\text{Ni}_{1-x}\text{Cr}_{2x/3}\text{O}$ islands. (b) Corresponding SAED pattern obtained from the rocksalt $\text{Ni}_{1-x}\text{Cr}_{2x/3}\text{O}$ – metal that shows cube-on-cube epitaxy.

Despite the successful preservation of the surface structure through cryogenic preparation and analysis, many unanswered questions remain about these complex systems. The literature suggests that chloride ions could be trapped in the hydroxide (substituting for OH^-) during aqueous corrosion [53, 58], which motivates further study. There are also many open issues as to whether the hydroxide phase is purely nickel hydroxide or whether it incorporates chromium and/or molybdenum. The valence states are also important to understand the electrochemical reactions, for instance whether one has Mo^{4+} or Ni^{3+} in the hydroxide. This merits further attention. Minor chemical and electronic fluctuations in the hydroxide have little effect on its structure and morphology, causing these details to be overlooked in diffraction-based studies such as this one. These effects will be studied in more detail and with more advanced methods in future work.

The approach is not without its limitations. For instance, specimen drift and charging remain a challenge in cryo-TEM [59]. Minor chemical fluctuations, such as the capture of chromium and molybdenum in the oxide and hydroxide, are often localized and would require high-resolution high-angle annular dark field imaging and energy dispersive X-ray spectroscopy (EDS). Identification of the valence states would require EELS. While EDS and EELS are standard chemical characterization techniques for TEM, considerable experimental design is required to ensure the collected spectra are representative of the hydrated alloy sample during cryo-TEM characterization. These challenges are being addressed with promising results [60]. The results presented in this paper are just the first steps in establishing a cryo-TEM based technique to understand early-stage oxidation processes.

5. Conclusions

With a combined cryo-FIB and cryo-TEM approach, a corroded NiCrMo alloy was investigated in a frozen-hydrated state during aqueous corrosion. NiCrMo half-discs were mechanically polished and ion milled prior to aqueous corrosion, and the resulting corroded specimens were immediately plunge-frozen using liquid nitrogen. Cryo-FIB milling thinned down the ice layer to electron transparency. Cryo-TEM imaging and electron diffraction then revealed the presence of rocksalt and polycrystalline $\beta\text{-Ni}_{1-x}\text{Cr}_{2x/3}(\text{OH})_2$ on the surface of the corroded NiCrMo, supporting that these phases were formed onto the alloy during aqueous corrosion in a Cl^- -containing electrolyte solution. The $\beta\text{-Ni}_{1-x}\text{Cr}_{2x/3}(\text{OH})_2$ phase, which has not been observed in previous TEM characterizations of corroded NiCrMo alloys, have multiple orientational relationships in the hydrated alloy sample. These complex orientational relationships between the oxides and hydroxides with the bulk metal were studied with SAED and DF imaging. We thereby established an efficient work flow which will allow detailed studies of orientational relationships in several materials systems undergoing aqueous corrosion.

Acknowledgments

The authors gratefully acknowledge funding from the Office of Naval Research MURI on contract no. N00014-16-1-2280 and the National Science Foundation on grant no. CMMI-1400618. Work at the Molecular Foundry was supported by the Office of Science, Office of Basic Energy Sciences, of the US Department of Energy under contract no. DE-AC02-05CH11231. We thank John R. Scully (University of Virginia) for providing the samples used in this study and Frances Allen (University of California, Berkeley) for helpful discussions.

References

- [1] D. Thierry, D. Persson, C. Leygraf, D. Delichère, S. Joiret, C. Pallotta, A.H.L. Goff, In-Situ Raman spectroscopy combined with X-ray photoelectron spectroscopy and nuclear microanalysis for studies of anodic corrosion film formation on Fe-Cr single crystals, *J. Electrochem. Soc.* 135 (1988) 305–310.
- [2] J.E. Maslar, W.S. Hurst, J.J. Bowers, J.H. Hendricks, M.I. Aquino, In situ Raman spectroscopic investigation of nickel hydrothermal corrosion, *Corrosion* 58 (2002) 225–231.
- [3] J.E. Maslar, W.S. Hurst, W.J. Bowers, J.H. Hendricks, E.S. Windsor, Alloy 600 aqueous corrosion at elevated temperatures and pressures: An In Situ Raman spectroscopic investigation, *J. Electrochem. Soc.* 156 (2009) C103–C113.
- [4] S. Yamamoto, H. Bluhm, K. Andersson, G. Ketteler, H. Ogasawara, M. Salmeron, A. Nilsson, In situ X-ray photoelectron spectroscopy studies of water on metals and oxides at ambient conditions, *J. Phys.* 20 (2008) 184025.
- [5] P. Jiang, J.L. Chen, F. Borondics, P.A. Glans, M.W. West, C.L. Chang, M. Salmeron, J.H. Guo, In situ soft X-ray absorption spectroscopy investigation of electrochemical corrosion of copper in aqueous NaHCO_3 solution, *Electrochem. Commun.* 12 (2010) 820–822.
- [6] I. Milosev, M. Metikos-Hukovic, H.H. Strehblow, Passive film on orthopaedic TiAlV alloy formed in physiological solution investigated by X-ray photoelectron spectroscopy, *Biomaterials* 21 (2000) 2103–2113.
- [7] P. Schmuki, S. Virtanen, A.J. Davenport, C.M. Vitus, Transpassive dissolution of Cr and sputter-deposited Cr oxides studied by in situ X-ray near-edge spectroscopy, *J. Electrochem. Soc.* 143 (1996) 3997–4005.
- [8] A. Davoodi, J. Pan, C. Leygraf, S. Norgren, Integrated AFM and SECM for in situ studies of localized corrosion of Al alloys, *Electrochimica Acta* 52 (2007) 7697–7705.
- [9] K. Kowal, J. DeLuccia, J. Josefowicz, C. Laird, G. Farrington, In situ atomic force microscopy observations of the corrosion behavior of aluminum-copper alloys, *J. Electrochem. Soc.* 143 (1996) 2471–2481.
- [10] F.A. Martin, C. Bataillon, J. Cousty, In situ AFM detection of pit onset location on a 304L stainless steel, *Corrosion Sci.* 50 (2008) 84–92.
- [11] D. Zuili, V. Maurice, P. Marcus, Surface structure of nickel in acid solution studied by in situ scanning tunneling microscopy, *J. Electrochem. Soc.* 147 (2000) 1393–1400.
- [12] T. Suzuki, T. Yamada, K. Itaya, In situ electrochemical scanning tunneling microscopy of Ni(111), Ni(100), and sulfur-modified Ni(100) in acidic solution, *J. Phys. Chem.* 100 (1996) 8954–8961.
- [13] A. Seyeux, V. Maurice, L.H. Klein, P. Marcus, In situ scanning tunnelling microscopic study of the initial stages of growth and of the structure of the passive film on Ni(111) in 1mM NaOH(aq), *J. Solid State Electrochem.* 9 (2005) 337–346.
- [14] J. Kunze, V. Maurice, L.H. Klein, H.H. Strehblow, P. Marcus, In situ STM study of the effect of chlorides on the initial stages of anodic oxidation of Cu(111) in alkaline solutions, *Electrochimica Acta* 48 (2003) 1157–1167.
- [15] C. Merola, H.-W. Cheng, K. Schwenzfeier, K. Kristiansen, Y.-J. Chen, H.A. Dobbs, J.N. Israelachvili, M. Valtiner, In situ nano- to microscopic imaging and growth mechanism of electrochemical dissolution (e.g., corrosion) of a confined metal surface, *Proc. Natl. Acad. Sci.* 114 (2017) 9541–9546.
- [16] J.Y. Huang, L. Zhong, C.M. Wang, J.P. Sullivan, W. Xu, L.Q. Zhang, S.X. Mao,

- N.S. Hudak, X.H. Liu, A. Subramanian, H. Fan, L. Qi, A. Kushima, J. Li, In situ observation of the electrochemical lithiation of a single SnO₂ nanowire electrode, *Science* 330 (2010) 1515–1520.
- [17] X.H. Liu, Y. Liu, A. Kushima, S. Zhang, T. Zhu, J. Li, J.Y. Huang, In situ TEM experiments of electrochemical lithiation and delithiation of individual nanostructures, *Adv. Energy Mater.* 2 (2012) 722–741.
- [18] M. Gu, L.R. Parent, B.L. Mehdi, R.R. Unocic, M.T. McDowell, R.L. Sacci, W. Xu, J.G. Connell, P. Xu, P. Abellan, X. Chen, Y. Zhang, D.E. Perea, J.E. Evans, L.J. Lauhon, J.G. Zhang, J. Liu, N.D. Browning, Y. Cui, I. Arslan, C.M. Wang, Demonstration of an electrochemical liquid cell for operando transmission electron microscopy observation of the lithiation/delithiation behavior of Si nanowire battery anodes, *Nano Lett.* 13 (2013) 6106–6112.
- [19] M.E. Holtz, Y. Yu, D. Gunceler, J. Gao, R. Sundararaman, K.A. Schwarz, T.A. Arias, H.D. Abruña, D.A. Muller, Nanoscale imaging of lithium ion distribution during in situ operation of battery electrode and electrolyte, *Nano Lett.* 14 (2014) 1453–1459.
- [20] Z. Zeng, W.I. Liang, H.G. Liao, H.L. Xin, Y.H. Chu, H. Zheng, Visualization of electrode-electrolyte interfaces in LiPF₆/EC/DEC electrolyte for lithium ion batteries via in situ TEM, *Nano Lett.* 14 (2014) 1745–1750.
- [21] R.L. Sacci, N.J. Dudney, K.L. More, L.R. Parent, I. Arslan, N.D. Browning, R.R. Unocic, Direct visualization of initial SEI morphology and growth kinetics during lithium deposition by in situ electrochemical transmission electron microscopy, *Chem. Commun.* 50 (2014) 2104–2107.
- [22] R.R. Unocic, R.L. Sacci, G.M. Brown, G.M. Veith, N.J. Dudney, K.L. More, F.S. Walden, D.S. Gardiner, J. Damiano, D.P. Nackashi, Quantitative electrochemical measurements using in situ ec-S/TEM devices, *Microsc. Microanal.* 20 (2014) 452–461.
- [23] S.W. Chee, S.H. Pratt, K. Hattar, D. Duquette, F.M. Ross, R. Hull, Studying localized corrosion using liquid cell transmission electron microscopy, *Chem. Commun.* 51 (2015) 168–171.
- [24] S.W. Chee, D.J. Duquette, F.M. Ross, R. Hull, Metastable structures in Al thin films before the onset of corrosion pitting as observed using liquid cell transmission electron microscopy, *Microsc. Microanal.* 20 (2014) 462–468.
- [25] D.J. Smith, M.R. McCartney, L.A. Bursill, The electron-beam-induced reduction of transition metal oxide surfaces to metallic lower oxides, *Ultramicroscopy* 23 (1987) 299–303.
- [26] H. Zheng, Y. Zhu, Perspectives on in situ electron microscopy, *Ultramicroscopy* 180 (2017) 188–196.
- [27] J. Dubochet, A.W. McDowell, Vitrification of pure water for electron-microscopy, *J. Microsc.* 124 (1981) RP3–RP4.
- [28] J. Dubochet, M. Adrian, J.-J. Chang, J.-C. Homo, J. Lepault, A.W. McDowell, P. Schultz, Cryo-electron microscopy of vitrified specimens, *Q. Rev. Biophys.* 21 (1988) 129–228.
- [29] M.J. Dobro, L.A. Melanson, G.J. Jensen, A.W. McDowell, Plunge freezing for electron cryomicroscopy, *Methods Enzymol.* 481 (2010) 63–82.
- [30] R.F. Thompson, M. Walker, C.A. Siebert, S.P. Muench, N.A. Ranson, An introduction to sample preparation and imaging by cryo-electron microscopy for structural biology, *Methods* 100 (2016) 3–15.
- [31] M. Schaffer, J. Mahamid, B.D. Engel, T. Laugks, W. Baumeister, J.M. Plitzko, Optimized cryo-focused ion beam sample preparation aimed at in situ structural studies of membrane proteins, *J. Struct. Biol.* 197 (2017) 73–82.
- [32] E. Villa, M. Schaffer, J.M. Plitzko, W. Baumeister, Opening windows into the cell: focused-ion-beam milling for cryo-electron tomography, *Curr. Opin. Struct. Biol.* 23 (2013) 771–777.
- [33] J.R. Hayes, J.J. Gray, A.W. Szmody, C.A. Orme, Influence of chromium and molybdenum on the corrosion of nickel-based alloys, *Corrosion* 62 (2006) 491–500.
- [34] A.K. Mishra, D.W. Shoesmith, Effect of alloying elements on crevice corrosion inhibition of nickel-chromium-molybdenum-tungsten alloys under aggressive conditions: An electrochemical study, *Corrosion* 70 (2014) 721–730.
- [35] F.H. Stott, G.C. Wood, J. Stringer, The influence of alloying elements on the development and maintenance of protective scales, *Oxidation of Metals* 44 (1995) 113–145.
- [36] D.L. Piron, E.P. Koutsoukos, K. Nobe, Corrosion behavior of nickel and inconel in acidic chloride solutions, *Corrosion* 25 (1969) 151–156.
- [37] R.S. Lillard, M.P. Jurinski, J.R. Scully, Crevice corrosion of alloy-625 in chlorinated ASTM artificial ocean water, *Corrosion* 50 (1994) 251–265.
- [38] R.W. Cairns, E. Ott, X-ray studies of the system nickel–oxygen–water. I. Nickelous oxide and hydroxide, *J. Am. Chem. Soc.* 55 (1933) 527–533.
- [39] N.N. Khoi, Growth and structure of nickel oxide on nickel crystal faces, *J. Electrochem. Soc.* 122 (1975) 1495–1503.
- [40] K. Hono, T. Iwata, M. Nakamura, H.W. Pickering, I. Kamiya, T. Sakurai, Atom-probe study of the initial-stage of selective oxidation of Ni from the Cu-Ni alloy system, *Surface Sci.* 245 (1991) 132–149.
- [41] X.X. Yu, A. Gulec, Q. Sherman, K. Lutton Cwalina, J.R. Scully, J.H. Perepezko, P.W. Voorhees, L.D. Marks, Nonequilibrium solute capture in passivating oxide films, *Phys. Rev. Lett.* 121 (2018) 145701.
- [42] L. Kjellqvist, M. Selleby, B. Sundman, Thermodynamic modelling of the Cr–Fe–Ni–O system, *Calphad* 32 (2008) 577–592.
- [43] A. Van der Ven, D. Morgan, Y.S. Meng, G. Ceder, Phase stability of nickel hydroxides and oxyhydroxides, *J. Electrochem. Soc.* 153 (2006) A210–A215.
- [44] R.S. McEwen, Crystallographic studies on nickel hydroxide and the higher nickel oxides, *J. Phys. Chem.* 75 (1971) 1782–1789.
- [45] D.S. Hall, D.J. Lockwood, C. Bock, B.R. MacDougall, Nickel hydroxides and related materials: A review of their structures, synthesis and properties, *Proc. R. Soc. A* 471 (2014) 20140792.
- [46] L.R. Comolli, R. Duarte, D. Baum, B. Luef, K.H. Downing, D.M. Larson, R. Csencsits, J.F. Banfield, A portable cryo-plunger for on-site intact cryogenic microscopy sample preparation in natural environments, *Microsc. Res. Technique* 75 (2012) 829–836.
- [47] M.J. Zachman, E. Asenath-Smith, L.A. Estroff, L.F. Kourkoutis, Site-specific preparation of intact solid-liquid interfaces by label-free in situ localization and cryo-focused ion beam lift-out, *Microsc. Microanal.* 22 (2016) 1338–1349.
- [48] G.C. Wood, B. Chattopadhyay, Transient oxidation of Ni-base alloys, *Corrosion Sci.* 10 (1970) 471–480.
- [49] P. Marcus, V. Maurice, Atomic level characterization in corrosion studies, *Philos. Trans. R. Soc. A* 375 (2017).
- [50] M. Chebeir, H. Liu, Oxidation of Cr(III)-Fe(III) mixed-phase hydroxides by chlorine: Implications on the control of hexavalent chromium in drinking water, *Environ. Sci. Technol.* 52 (2018) 7663–7670.
- [51] H. Bode, K. Dehmelt, J. Witte, Zur kenntnis der nickelhydroxidelektrode—I. Über das nickel (II)-hydroxidhydrat, *Electrochimica Acta* 11 (1966) 1079–1087.
- [52] P. Oliva, J. Leonardi, J.F. Laurent, C. Delmas, J.J. Braconnier, M. Figlarz, F. Fievet, A. Deguibert, Review of the structure and the electrochemistry of nickel hydroxides and oxy-hydroxides, *J. Power Sources* 8 (1982) 229–255.
- [53] P. Marcus, J.M. Herbelin, The entry of chloride ions into passive films on nickel studied by spectroscopic (ESCA) and nuclear (36Cl radiotracer) methods, *Corrosion Sci.* 34 (1993) 1123–1145.
- [54] H.-H. Strehblow, Passivity of metals, *Adv. Electrochem. Sci. Eng.* 8 (2002) 271–374.
- [55] S. Haupt, H.H. Strehblow, Corrosion, layer formation, and oxide reduction of passive iron in alkaline-solution—A combined electrochemical and surface analytical study, *Langmuir* 3 (1987) 873–885.
- [56] V. Maurice, P. Marcus, Passive films at the nanoscale, *Electrochimica Acta* 84 (2012) 129–138.
- [57] D.D. Macdonald, Passivity—the key to our metals-based civilization, *Pure Appl. Chem.* 71 (1999) 951–978.
- [58] M.R. Gilberg, N.J. Seeley, The identity of compounds containing chloride ions in marine iron corrosion products: A critical review, *Stud. Conservation* 26 (1981) 50–56.
- [59] C.J. Russo, R. Henderson, Charge accumulation in electron cryomicroscopy, *Ultramicroscopy* 187 (2018) 43–49.
- [60] M.J. Zachman, Z. Tu, S. Choudhury, L.A. Archer, L.F. Kourkoutis, Cryo-STEM mapping of solid-liquid interfaces and dendrites in lithium-metal batteries, *Nature* 560 (2018) 345–349.